CONSTITUTIVE MODEL FOR DAMAGED BOROSILICATE GLASS

Sidney Chocron, James D. Walker, Arthur E. Nicholls, Charles E. Anderson, Kathryn A. Dannemann
Southwest Research Institute
PO Drawer 28510
San Antonio, Texas 78228-0510

ABSTRACT

An experimental technique developed in a previous paper, and consisting of testing a predamaged specimen inside a steel sleeve, is used to obtain the data to develop the constitutive equations (elastic and plastic behavior) for Borofloat® 33 glass. The glass was chosen as the specimen because it is easy to fail in that configuration. This paper first briefly summarizes the experimental technique and then shows that, if the specimen follows a Drucker-Prager plasticity model it is possible to determine, with the help of an analytical model, the elastic and plastic constants from the slopes of the axial stress vs. axial strain and axial stress vs. hoop strain curves measured in the laboratory tests. The paper determines the constants and shows how the model compares with the test data available so far. The analytical model is verified with the help of LS-DYNA in 2-D and 3-D numerical simulations. The analytical and numerical models allow a double check of different assumptions and confirm that the experimental technique is a valid procedure to determine the elastic and plastic constants. The constants can then be used in very different computations like ballistic penetration.

INTRODUCTION

An experimental technique consisting of testing a predamaged specimen of SiC-N inside a steel sleeve allowed the determination of the constitutive elastic and plastic equations for SiC-N as shown in [1]. An analytical model was simultaneously developed [2] to help in the interpretation of the elastic part of the load. The same experimental technique is used in this work, see [3], but with predamaged glass (Borofloat® 33) specimens. This time, to seek a more complete interpretation of the tests, an elasto-plastic analytical model was developed together with numerical simulations using LS-DYNA in two and three dimensions.

EXPERIMENTAL TECHNIQUE

The experimental technique is thoroughly described in the paper by Dannemann et al. [1] so it will only be briefly summarized here for completeness. A predamaged borosilicate glass (Borofloat® 33) specimen with cylindrical shape is placed inside an annular steel (Vascomax) sleeve and stresses are applied at both ends of the specimen by means of an MTS machine. During the test the axial stress and strain of the specimen are being recorded. The hoop strain of the sleeve is also measured with a strain gage placed on its outer diameter and centered with the specimen, see Figure 1.

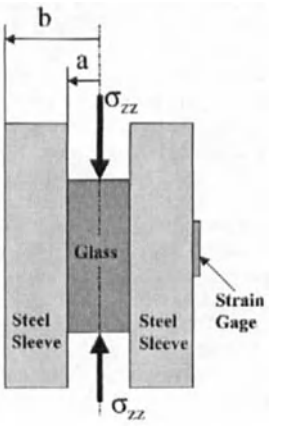

Figure 1: Experimental set-up

If the sleeve does not yield during the test a simple analytical model relates the hoop strain in the outer diameter with the confining pressure and, in general, the whole stress and strain state is known in both the sample and the sleeve.

There are some concerns with the experimental technique that will be addressed with the numerical and analytical models:

1) Friction between the specimen and the sleeve might artificially increase the axial strain.
2) There might be a hoop strain gradient along the axis direction in the outer diameter of the sleeve. This may cause non-uniform loading of the specimen. Since the equivalent stress is the difference of two large quantities, small errors can result in misinterpretation of the results.
3) The sleeve might be yielding at some point during the experiment, invalidating the elastic assumption.

The analytical and numerical models will also be a helpful tool to answer some interesting questions concerning the glass:

1) Does the glass bulk when it fails?
2) Do the elastic constants change from intact to predamaged glass?
3) Do the elastic constants change when cycling or further damaging the glass?
4) Does the glass fail catastrophically, or is there inelastic-plastic flow?
5) Can the inelastic-plastic flow of the glass be appropriately modeled (numerically or analytically)?
6) Can failure of the glass be modeled?

In this context the word "failure" or "catastrophic failure" means a sudden change in the elastic and/or the plastic constants that describe the material.

ELASTO-PLASTIC ANALYTICAL MODEL

An analytical model for the elastic loading was developed in a previous paper [2]. The analytical model provided a fast and easy way to estimate the elastic modulus and Poisson's ratio of the specimen during the elastic loading by means of a linear system of four equations but it could not be used when the specimen started to flow plastically.

In this paper the model has been completely rewritten in terms of increments of elastic and plastic strains. This allows the explicit calculation of the slopes of the elastic and plastic branches of the Stress vs. Strain and Stress vs. Hoop Strain curves from the elastic constants and the assumed plastic constitutive equation. In other words, the slopes measured during the tests give directly the constitutive constants of the specimen, as it will be shown.

Figure 2 shows an idealized interpretation of the test results done in [3] although only the loading branch is shown. Even though the glass tested is predamaged it is assumed in this paper that an elastic branch (1 and 1′ in Figure 2) of deformation does exist because, as shown in [3], a load-unload cycle returns to zero strain if the yield point is not attained. It is also assumed that at some point yielding starts with a small change in slope (2 and 2′), and if unload happens, a permanent deformation could be measured. During plastic flow the behavior of the material is assumed to be smooth, its elastic constants should remain the same and the yield strength is assumed to follow a Drucker-Prager model ($Y=Y_0+\beta P$, where Y_0 and β are material constants). It is known that cracks initiate and grow even when stresses as small as 500 MPa are applied making it "risky" to argue that the specimens remain elastic or deform plastically. Still the authors think that, when the material is confined (as in these experiments or in ballistic penetration), even if some limited crack growth happens the specimen, in the macroscale, behaves as if it were elastic and/or plastic below a threshold where sudden jumps appear, see [3].

Tests also show sudden jumps in both hoop strain and axial strain where slopes 3 and 3′ are virtually horizontal. That part of the test is not addressed in this paper and is the subject of further research.

The analytic model is fully explained in the appendix of this paper. To make the paper less cumbersome to read only the main assumptions and results of the model will be explained in the main part of the paper.

Assumptions

The problem is assumed to be axisymmetric and the radial displacement fields in the specimen and sleeve follow the equation $u_r(r) = Ar + B/r$, where A and B are determined by the boundary conditions

for each stress σ_{zz}, and are different for the specimen and sleeve. The specimen is assumed to smoothly slip in the sleeve so no friction is considered between the sleeve and the specimen (this assumption is discussed later in the paper). The constitutive equations of the specimen are Hooke's law and the Drucker-Prager model. A uniform strain is assumed in the axial direction, i.e., the specimen and sleeve do not bend. The stress in the axial direction in the sleeve is assumed to be zero (which is a consequence of the no friction assumption).

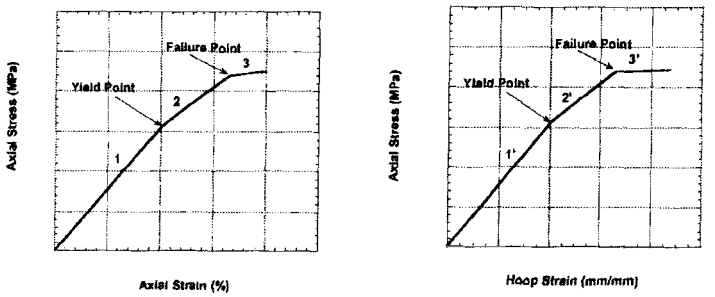

Figure 2: Idealized stress-strain curves obtained from the testing.

Given all the above assumptions it is possible to explicitly write slopes 1, 1′, 2, 2′ as a function of the elastic and plastic constants of specimen and sleeve:

Slope 1, which happens during elastic deformation, is given by (Eq. 29):

(Eq. 1)
$$\left.\frac{d\sigma_z}{d\varepsilon_z}\right|_{elastic} = \frac{2\lambda d\varepsilon_r + (\lambda + 2\mu) d\varepsilon_z}{d\varepsilon_z}$$

where λ and μ are the Lamé constants for the specimen and $d\varepsilon_z$ is the applied (known) strain in the specimen. Using (Eq. 30):

(Eq. 2)
$$\text{slope } 1 = \left.\frac{d\sigma_z}{d\varepsilon_z}\right|_{elastic} = \frac{2\lambda^2}{C' - 2(\lambda+\mu)} + (\lambda + 2\mu)$$

C' is a constant that relates the radial stress (or confinement pressure) in the specimen with the radial displacement of the inner part of the sleeve. C' only depends on the elastic constants of the sleeve and its geometry and is explicitly given by (Eq. 25) in the Appendix.

Similarly, slope 2 is given by (Eq. 40) in the appendix:

(Eq. 3)
$$\text{slope } 2 = \left.\frac{d\sigma_z}{d\varepsilon_z}\right|_{plastic} = \beta' C' \left(\gamma\left(\frac{1}{2} - \delta\right) - \frac{1}{2}\right)$$

where β', γ and δ are given, respectively, in (Eq. 33), (Eq. 34) and (Eq. 35).

Combining (Eq. 32) with (Eq. 30) it is possible to write slope 1′:

(Eq. 4)
$$\text{slope } 1' = \left.\frac{d\sigma_z}{d\varepsilon_\theta}\right|_{\substack{elastic \\ r=b}} = \frac{2\lambda^2 + (\lambda+2\mu)(C' - 2(\lambda+\mu))}{\lambda\left(A' + \frac{B'}{b^2}\right)}$$

A′ and B′ are constants that depend on the elastic constants of the sleeve, λ′ and μ′, and the geometry of the sleeve, see (Eq. 22) and (Eq. 23). For the plastic part of the stress vs. hoop-strain curve:

(Eq. 5) $$\text{slope } 2' = \left.\frac{d\sigma_z}{d\varepsilon_\theta}\right|_{\substack{\text{plastic}\\ r=b}} = \frac{\beta' C'}{\left(A' + \frac{B'}{b^2}\right)}$$

Once the slopes are measured from the experiments (Eq. 2) through (Eq. 5) provide four equations with three unknowns, the elastic constants of the specimen, λ, μ and the plastic constant of the specimen, β. The strength at zero pressure Y_0 does not affect the slopes but determines the onset of plastic flow and which is how it will be determined.

NUMERICAL SIMULATIONS WITH LS-DYNA

Verification of the model is usually done in the SwRI® Engineering Dynamics Department with the "triad" approach. If tests, analytical model and numerical simulations give the same results the analytical model is considered verified, and its assumptions valid. Numerical simulations in 2-D and 3-D were performed with LS-DYNA®, a finite element code developed by LSTC. The 2-D computation did not allow a Drucker-Prager strength model so only the elastic part was implemented. In the 3-D simulations there were 14 brick elements across the radius. The grid was generated with Truegrid®. The material properties used are summarized in Table 1. The penalty factor in the "contact" card was increased to 30 to avoid any interpenetration of the materials and to be able to see some measurable hoop strain in the outer part of the sleeve right from the start of the load.

Table 1: Material properties used in the numerical and analytical simulations

Specimen (damaged glass) properties		Sleeve (Vascomax) properties	
Elastic Modulus (GPa)	59	**Elastic Modulus (GPa)**	205
Poisson's ratio	0.19	**Poisson's ratio**	0.28
Y_0 (MPa)O	250	**Inner radius (mm)**	3.14
β	1.63	**Outer radius (mm)**	6.31
Length (mm)	12.65	**Length (mm)**	22.24

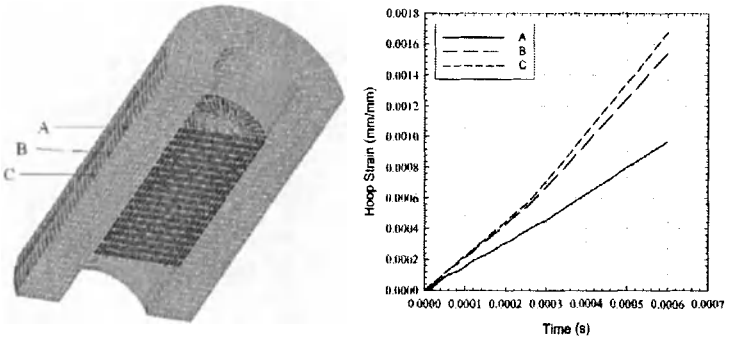

Figure 3: a) Mesh used in LS-DYNA for verification of the analytical model, b) hoop strain at three different locations in the outer surface of the sleeve

Figure 3a) shows half of the mesh used in the 3-D version of LS-DYNA. A boundary condition in displacement was applied at the top of the specimen while the motion of bottom of the specimen was constrained in the axial direction. No friction between specimen and sleeve was considered for the verification of the analytical model.

Hoop strain gradient in the sleeve

One of the concerns of the experiment is the hoop strain gradient that happens in the outer part of the sleeve. Because the sleeve is longer than the specimen it is expected that the strains are larger in the middle vertical plane (perpendicular to the axis) of the sleeve. Figure 3b) shows strains for three tracers located on the outer surface of the sleeve, at different heights. A is located in the plane that contains the top surface of the specimen. C is located in the middle plane of the specimen and B is halfway in between. Indeed the gradient is important and care needs to be taken to place the strain gage (3.18 mm height in the axial direction and 9.6 mm long in the hoop direction) accurately in the middle plane. New tests are being prepared with a shorter sleeve to decrease the strain gradient. Also smaller strain gages will be used to avoid "averaging" through a wide area of the sleeve.

Influence of friction between sleeve and specimen.

The friction coefficient, f, between the sleeve and the specimen was set to 0.1 and 1 in two different runs to study its influence in the interpretation of the tests. Figure 4 shows how the results change when friction is present.

For a friction coefficient f=0.1, the elastic slope of the test is only affected slightly so the Young modulus and Poisson's ratio would not change considerably. The yield point is significantly reduced (from 1.4 to 1.1 GPa), so a friction coefficient would artificially decrease the Y_0 measured in the test resulting in a misinterpretation of the data. The plastic slope is also affected but only in a degree similar to the scatter found during the experiments. The authors think that a friction coefficient on the order of 0.1 or less would be acceptable since the test would still give meaningful results, although it would systematically slightly increase the Poisson's ratio and decrease the slope of the Drucker-Prager curve.

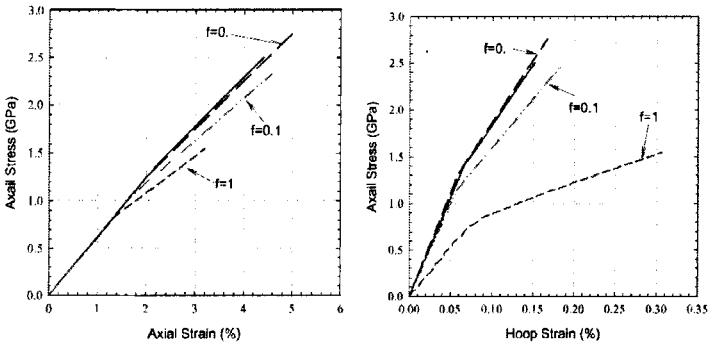

Figure 4: Parametric study with LS-DYNA of the influence of the friction coefficient f. The red continuous line is the analytical model without friction.

A higher friction coefficient like f=1 clearly has a tremendous impact on the tests results, see again Figure 4, invalidating the assumptions and making the results very difficult to interpret. Since the sleeve would be supporting part of the axial load transmitted from the specimen to the sleeve through friction, it should be possible to measure during the experiment an axial strain in the outer part of the sleeve. In fact the numerical simulations show that the axial stress level in the outer surface could reach around 600 MPa

(or 0.1 % strain) for f=1, a value that should be easy to measure. In the future some tests with a vertical strain gage will be performed to evaluate if friction is important.

RESULTS AND DISCUSSION

Analysis of the experimental results using the analytical model

This part is work in progress but the results obtained so far will be presented. Four predamaged glass specimens have been tested in the confinement sleeve and analyzed by the authors. Each test consisted of multiple load-unload cycles. An example of the axial stress vs. axial strain and vs. hoop strain curves obtained during the tests are shown in Figure 5. The slopes (1,1',2,2'), identified in Figure 2, for all the load cycles were measured. Slopes 1 and 2 in the axial stress vs. axial strain curve are simple to identify and measure. The axial stress vs. hoop strain curve starts with a bending that makes it much more difficult to identify slopes 1' and 2'. The cause for the initial bending (a linear rise is expected) is unknown. More testing is underway with thinner and shorter sleeves to ensure that there is no contact between sleeve and anvils used to exert the axial stress and that hoop strain measurement is being done properly.

The slopes measured in each loading cycle are shown in Table 2. Slopes 2 and 2'do not always exist, because the test remained elastic, as in the first cycle. Sometimes failure hides the slopes, for example in cycles 5 and 6, so "n/a" (not available) appears in lieu of a value. The slopes were measured by fitting a linear equation to the part of the curve of interest, usually obtaining correlation coefficients of 0.999 or more.

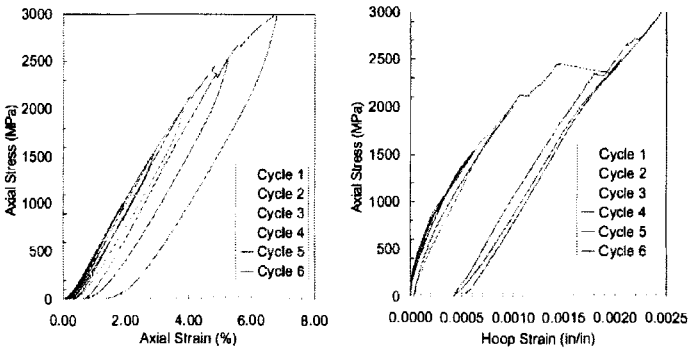

Figure 5: Test BF-8, a) stress vs. axial strain, b) stress vs. hoop strain.

The slopes, shown in Table 2, can be used as input of the analytical model to find E,ν and β. Depending on the cycle and test used (or by using the average) the modulus was found to range from 55 to 63 GPa, the Poisson's ratio from 0.12 to 0.19, and β from 1.6 to 2.0. The table also presents the material constants (Lamé constants, λ, μ, Slope of Drucker-Prager, β, Young Modulus, E, Shear Modulus, G and Poisson's ratio, ν) calculated from the model using each cycle slope. The properties of intact unconfined glass measured with ultrasonic and MTS procedures are also included in Table 2 for comparison.

Table 2: Slopes of the elastic and plastic branches for test BF-8. Material constants inferred from the analytical model are also shown.

	Slope 1 (GPa)	Slope 2 (GPa)	Slope 1′ (TPa)	Slope 2′ (TPa)	Material constants calculated with model					
					λ (GPa)	μ (GPa)	β	E (GPa)	G (GPa)	ν
Cycle 1	55.84	n/a	n/a	n/a	-	-	-	-	-	-
Cycle 2	61.01	56.37	2.38	2.00	12.00	25.35	2.01	58.84	25.35	0.16
Cycle 3	61.58	53.88	1.90	1.59	13.72	25.02	1.82	58.90	25.02	0.18
Cycle 4	61.96	49.33	1.69	1.33	12.98	25.46	1.66	59.52	25.46	0.17
Cycle 5	60.56	n/a	1.62	n/a	-	-	-	-	-	-
Cycle 6	60.35	n/a	1.64	n/a	-	-	-	-	-	-
Average	61.09	53.19	1.85	1.64	12.71	25.13	1.85	58.70	25.13	0.17
Intact glass, ultrasonic measurement in the laboratory [4]								62.0-62.5	25.8-26.1	.194-.207
Intact glass, MTS measurement in the laboratory								57.7-62.3	-	0.16-0.19

To better assess the sensitivity of the experiment, Figure 6 presents the material constants inferred from tests BF-8, BF-11, BF-14, and BF-16 in a graphic form. Each symbol represents the values inferred from one cycle, so the plot is actually showing how the modulus and Poisson's ratio evolve during the test. The scatter in both elastic and shear modulus is reasonable with a maximum of around ±10%. The Poisson's ratio is more sensitive and has a larger scatter. Tests BF-8, 11 and 16 were similar in their procedure, increasing the final stress at each cycle. Test BF-14 was special in the sense that all the cycles went up to 2.5 GPa. The authors opinion is that there is no clear trend up or down for the moduli or Poisson's ratio. The scatter seems random supporting the fact that the elastic constants seem to stay the same, but more tests are needed to reach a final conclusion.

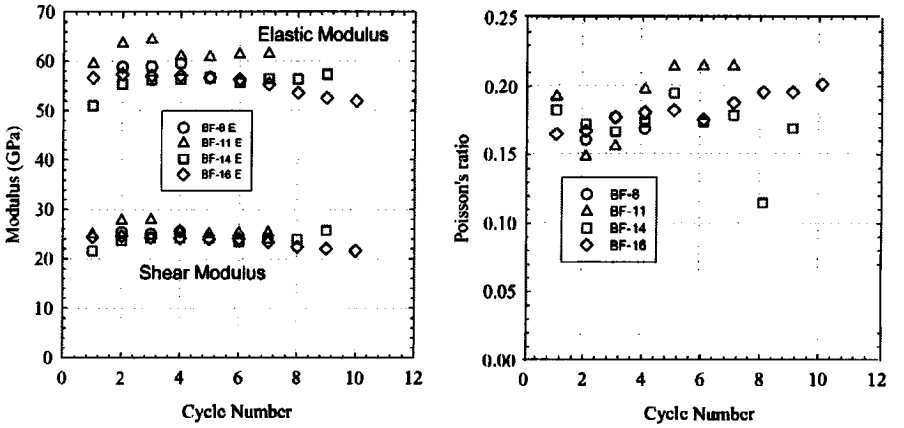

Figure 6: a) Young Modulus and Shear Modulus evolution for each cycle inferred (one symbol per cycle) from the analytical model, four different tests (BF-8, 11, 14 and 16) shown, b) same for the Poisson's ratio.

Verification of the analytical model

Figure 7 compares the results of the analytical and numerical model showing that both give very similar results. The slight differences are thought to be of numerical origin. It is very difficult to have a perfect contact between the specimen and the sleeve because, for example, the mesh of the specimen is

not perfectly circular and has "corners". Nevertheless both elastic and plastic slope match very well and the authors think that the analytical model has been verified.

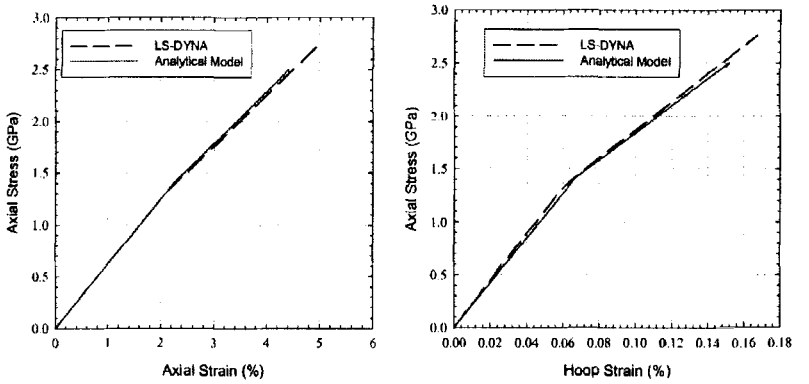

Figure 7: Verification of the analytical model by comparison with LS-DYNA results. a) Axial stress vs. axial strain, b) axial stress vs. hoop strain.

Does the sleeve yield during the test?

The equivalent stress is maximum in the inner part of the sleeve. Hence yielding will initiate in the inner radius of the sleeve. According to the analytical model, for the geometry presented in Table 1, the sleeve would start to yield for a hoop strain of 0.3 %. This corresponds to a confinement pressure of around 800 MPa and a pressure in the specimen of around 1.7 GPa (remember the specimen has the added component of the axial stress which the sleeve does not). Also, if the sleeve yields, the axial stress measured by the MTS should go flat. The model and the postmortem analysis confirm that the sleeve is not yielding during the test if hoop strains are kept below 0.3%.

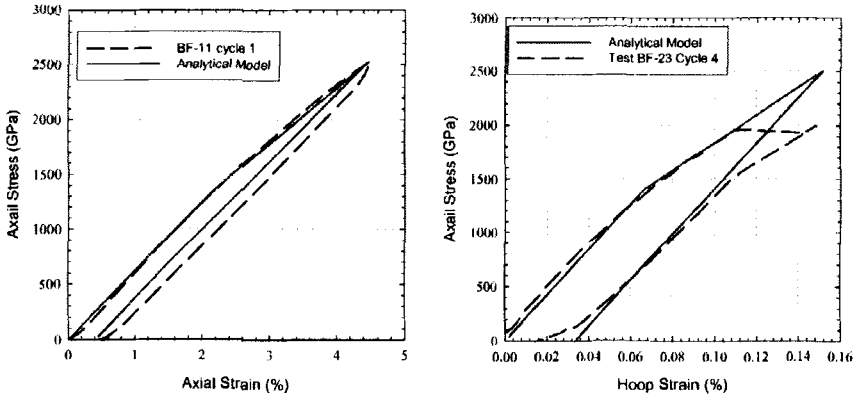

Figure 8: Comparison of analytical and experimental results for test BF-11. a) Axial stress vs. axial strain curve, only the first cycle is shown for clarity. b) Axial stress vs. hoop strain

Comparison of the analytical elasto-plastic model with the experimental results

Variability in the experimental results makes the determination of a set of constants a difficult task that should probably take a statistical approach. But the number of experiments is still not large enough to make a statistical determination of the constants. The following results can be considered an exercise to at least know an approximated value for β and Y_0. The exercise selected consists of loading the sample up to 2.5 GPa to make it go through the elastic and plastic branches and then unload. Similar branches were selected from the experimental results to compare with the analytical model. Figure 8 compares the model and the test and cycle selected. Although it is relatively straightforward to match the axial stress vs. strain load curve, the hoop strain is much more difficult because of the initial non-linearity and the steps (interpreted as failures) that happen. Nevertheless, the match with the test is good indicating that the material constants used for the simulations are at least realistic.

Volume change when the specimen fails

The volume of the specimen is known at any time during the test with the help of the strain gage placed in the sleeve and (Eq. 32) and (Eq. 15), which only involve the elastic sleeve. The change of volume ΔV measured in the test can be compared with the change of volume predicted by the model, which is of elastic origin. If both ΔV were the same, then the volume change is due to elastic compression and failure does not affect the volume.

Figure 9 compares ΔV for the model and test BF-11. The first cycle of the test is not shown because it reached very low stress. The following two cycles are shown but are shifted 0.7% to compensate for the non-linear initial part. Clearly ΔV is very similar for both, leading to the conclusion that, since the postmortem analysis of the specimen shows failure, failure does not change the volume.

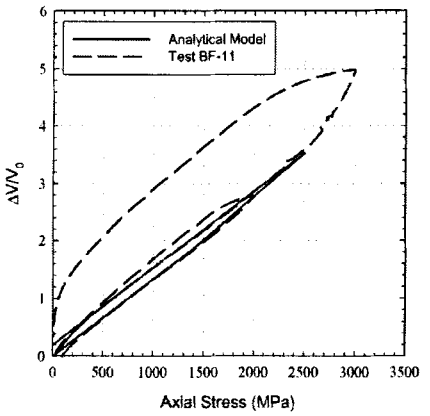

Figure 9 Comparison of the change of volume ΔV calculated with the model and ΔV measured during the test

Constitutive model

The ultimate objective of the project is to find a constitutive equation for damaged glass that could be used in numerical models to predict ballistic results. The results are still preliminary but the elastic constants range found in this paper is: E = 54-62 GPa, and ν = 0.16-0.2, meaning that the elastic constants of damage glass are very similar to the intact constants. The plastic part (Drucker Prager) constants range is: Y_0 = 250 MPa, and β = 1.6 – 2.0. It is expected that the constant range will vary a little during the ongoing research and when more experimental results (for example with thinner and shorter sleeves to be used) become available.

SUMMARY AND CONCLUSIONS

This work has shown that testing predamaged specimens in a confined sleeve is a sound experimental technique to determine the constitutive equation (elastic and plastic parts) of the specimen. With the help of the analytical and numerical models developed it is straightforward to interpret the results of the experiments and show that the assumptions are realistic and the constants obtained useful.

ACKNOWLEDGMENT

The authors would like to acknowledge Doug Templeton from TARDEC for his support and helpful discussions.

APPENDIX TO THE ELASTO-PLASTIC ANALYTICAL MODEL

The assumed Drucker-Prager constitutive equation during plastic deformation is of the form:

(Eq. 6) $$Y = Y_0 + \beta P$$

where Y is the yield strength, Y_0 the tensile strength at zero pressure, β the slope and P the pressure in the specimen.

Since there is cylindrical symmetry radial and hoop stresses are the same ($\sigma_r = \sigma_\theta$) so the equivalent stress in the specimen can be written, assuming shear stresses are zero:

(Eq. 7) $$\sigma_{eq} = \sqrt{3J_2} = |\sigma_r - \sigma_z|$$

and the yield condition in incremental form is:

(Eq. 8) $$d\sigma_r - d\sigma_z = \beta\left(-\frac{1}{3}d\sigma_z - \frac{2}{3}d\sigma_r\right)$$

Stresses are negative in compression so since σ_z is expected to be bigger than σ_r in absolute value, σ_r-σ_z is expected to be positive. From Hooke's law the incremental stresses can be written:

(Eq. 9) $$(\lambda + 2\mu)\, d\varepsilon_z^e + 2\lambda d\varepsilon_r^e = d\sigma_z$$

(Eq. 10) $$2(\lambda + \mu)\, d\varepsilon_r^e + \lambda d\varepsilon_z^e = d\sigma_r$$

where again it is assumed that $d\varepsilon_r$=$d\varepsilon_\theta$ and $d\varepsilon^e$ denotes elastic strain. λ and μ are the Lamé constants for the specimen material.

For the plastic strains in the specimen, conservation of volume yields:

(Eq. 11) $$2\ d\varepsilon_r^p + d\varepsilon_z^p = 0$$

And the total strain is given by elastic plus plastic strain:

(Eq. 12) $$d\varepsilon_z = d\varepsilon_z^p + d\varepsilon_z^e$$

(Eq. 13) $$d\varepsilon_r = d\varepsilon_r^p + d\varepsilon_r^e$$

Assuming the friction is small between the specimen and the sleeve, the sleeve exerts only a radial stress on the specimen, which will be shown below to be proportional to the displacement of the inner radius of the sleeve:

(Eq. 14) $$d\sigma_r = C'\frac{d\bar{u}_r}{a}$$

where C' is a proportionality constant that only depends on the elastic constants of the sleeve and its inner and outer radius. The bar on the u_r denotes that u_r is the displacement of the inner radius of the sleeve, i.e. $\bar{u}_r \equiv u_r(r = a)$. Note that σ_r is uniform in the specimen (not in the sleeve).

The last equation needed is the relation between the radial strain and the displacement of the inner radius of the sleeve that, assuming small displacements is:

(Eq. 15) $$d\bar{u}_r = a\ d\varepsilon_\tau\big|_{r=a}$$

(Eq. 8) through (Eq. 15) constitute a system of eight equations with eight unknowns: $d\sigma_{rr}$, $d\sigma_{zz}$, $d\varepsilon_z^e$, $d\varepsilon_z^p$, $d\varepsilon_r^e$, $d\varepsilon_r^p$, $d\varepsilon_r$, $d\bar{u}_r$, with $d\varepsilon_z$ given applied to the end of the specimen.

Determination of the proportionality constant C'

In this section the objective is to find the stress in the sleeve as a function of the displacement of the inner radius of the sleeve. The displacement field assumed is of the form [2]:

(Eq. 16) $$u_r = Ar + \frac{B}{r}$$

where A and B are constants in the sleeve, to be determined for each loading condition, and r is the distance between the axis and any point in the sleeve where the displacement is being asked. The boundary conditions for the sleeve are: 1) a given displacement in the inner radius, 2) stress free in the outer radius and 3) the stress in the axial direction in the sleeve is zero

(Eq. 17) $$u_r(r=a) = \bar{u}_r$$

(Eq. 18) $$\sigma_r(r=b) = 0$$

(Eq. 19) $$\sigma_z(r) = 0$$

where the stresses are given, anywhere in the sleeve by (see [2]):

(Eq. 20) $$\sigma_r = (\lambda' + 2\mu')\varepsilon_r + \lambda'\varepsilon_{\theta\theta} + \lambda'\varepsilon_z = (\lambda' + 2\mu')\left(A - \frac{B}{r^2}\right) + \lambda'\left(A + \frac{B}{r^2}\right) + \lambda'\varepsilon_z$$

(Eq. 21) $$\sigma_z = \lambda'\varepsilon_{rr} + \lambda'\varepsilon_{\theta\theta} + (\lambda' + 2\mu')\varepsilon_z = \lambda'\left(A - \frac{B}{r^2}\right) + \lambda'\left(A + \frac{B}{r^2}\right) + (\lambda' + 2\mu')\varepsilon_z$$

λ' and μ' are the Lamé constant of the sleeve.
Applying the boundary conditions to the two last equations gives the constants A and B:

(Eq. 22) $$A = A'\frac{\bar{u}_r}{a} \quad \text{where} \quad A' \equiv \frac{(\lambda' + 2\mu')\, a^2}{b^2(3\lambda' + 2\mu') + a^2(\lambda' + 2\mu')}$$

(Eq. 23) $$B = B'\frac{\bar{u}_r}{a} \quad \text{where} \quad \frac{B'}{a^2} = \frac{(3\lambda' + 2\mu')\, b^2}{b^2(3\lambda' + 2\mu') + a^2(\lambda' + 2\mu')}$$

C′ comes from finding the radial stress in the inner diameter of the sleeve:

(Eq. 24) $$\sigma_r(r=a) = 2\left((\lambda' + \mu')\, A' - \mu\frac{B'}{a^2}\right)\frac{\bar{u}_r}{a}$$

C′ is defined as:

(Eq. 25) $$C' \equiv 2\left((\lambda' + \mu')\, A' - \mu\frac{B'}{a^2}\right)$$

so that:

(Eq. 26) $$\sigma_r(r=a) = C'\frac{\bar{u}_r}{a} \quad \text{or} \quad d\sigma_r(r=a) = C'\frac{d\bar{u}_r}{a}$$

Again note that if r=a the radial stress in the specimen (which is constant in the specimen) is equal to that of the sleeve.
So the constants A′, B′, and C′ are all known and functions of the elastic constants of the sleeve and its inner and outer radius. Consequently the radial stress is easily calculated with (Eq. 20). The radial and hoop strain can be calculated from:

(Eq. 27) $$\varepsilon_r = \frac{\partial u_r}{\partial r} = \left(A' - \frac{B'}{r^2}\right)\frac{\bar{u}_r}{a} \quad \text{or} \quad d\varepsilon_r = \left(A' - \frac{B'}{r^2}\right)\frac{d\bar{u}_r}{a}$$

(Eq. 28) $$\varepsilon_\theta = \frac{u_r}{r} = \left(A' + \frac{B'}{r^2}\right)\frac{\bar{u}_r}{a} \quad \text{or} \quad d\varepsilon_\theta = \left(A' + \frac{B'}{r^2}\right)\frac{d\bar{u}_r}{a}$$

Explicit solution while the specimen remains elastic

Let's find explicitly stresses and strains in the specimen and the sleeve while the specimen is elastic. From Hooke's law it is possible to write:

(Eq. 29) $$\begin{cases} d\sigma_r = 2(\lambda + \mu)d\varepsilon_r + \lambda d\varepsilon_z \\ d\sigma_\theta = d\sigma_r \\ d\sigma_z = 2\lambda d\varepsilon_r + (\lambda + 2\mu)d\varepsilon_z \end{cases}$$

where $d\varepsilon_z$ is given.

Since $d\sigma_r = C'd\bar{u}_r/a$, which is constant in the specimen, and, from the definition of radial strains and for small displacements, $d\bar{u}_r = a d\varepsilon_r$, it is possible to find, using the first of (Eq. 29):

(Eq. 30) $$d\varepsilon_r = \frac{\lambda}{C' - 2(\lambda + \mu)}d\varepsilon_z$$

which is constant in the specimen because the displacement field u_r in the specimen is assumed to be proportional to r so $\varepsilon_r(r)$=constant. (Eq. 30) allows calculating all the stresses in the specimen with (Eq. 29), for a given $d\varepsilon_z$.

An interesting quantity to calculate is the hoop strain in the outer part of the sleeve, which is measured with a strain gage during the tests. From the displacement field of the sleeve, it is possible to write, anywhere in the sleeve:

(Eq. 31) $$d\varepsilon_\theta^{sleeve} = \left(A' + \frac{B'}{r^2}\right)\frac{d\bar{u}_r}{a} = \left(A' + \frac{B'}{r^2}\right) d\varepsilon_r\Big|_{r=a}^{specimen}$$

(Eq. 32) $$d\varepsilon_\theta^{sleeve}\Big|_{r=b} = \left(A' + \frac{B'}{b^2}\right) d\varepsilon_r\Big|_{r=a}^{specimen}$$

Explicit solution while the specimen is deforming plastically

All the unknowns discussed above can be explicitly solved. First define some convenient constants:

(Eq. 33) $$\beta' \equiv \frac{1+\frac{2}{3}\beta}{1-\frac{1}{3}\beta}$$

where it is recalled that β is the slope of the yield strength as a function of pressure.

(Eq. 34) $$\delta \equiv \frac{\lambda(\beta'-1)-2\mu}{2(\lambda(\beta'-1)+\beta'\mu)}$$

where λ and μ are the Lamé constants of the specimen.

(Eq. 35) $$\gamma \equiv \frac{C'}{2\left(2\delta(\lambda+\mu)-\lambda+C'\left(\frac{1}{2}-\delta\right)\right)}$$

Given the above constants it is possible to explicitly write the unknowns as a function of $d\varepsilon_z$, the applied axial strain:

(Eq. 36) $$d\varepsilon_z^e = \gamma d\varepsilon_z$$

(Eq. 37) $$d\varepsilon_r^e = -\gamma\ \delta\ d\varepsilon_z$$

(Eq. 38) $$d\varepsilon_r = \left(\gamma\left(\frac{1}{2}-\delta\right)-\frac{1}{2}\right)d\varepsilon_z$$

(Eq. 39) $$d\sigma_r = C'\ d\varepsilon_r = C'\left(\gamma\left(\frac{1}{2}-\delta\right)-\frac{1}{2}\right)d\varepsilon_z$$

(Eq. 40) $$d\sigma_z = \beta'\ d\sigma_r = \beta' C'\left(\gamma\left(\frac{1}{2}-\delta\right)-\frac{1}{2}\right)d\varepsilon_z$$

(Eq. 41) $$d\bar{u}_r = a\ d\varepsilon_r = a\left(\gamma\left(\frac{1}{2}-\delta\right)-\frac{1}{2}\right)d\varepsilon_z$$

REFERENCES

1. Kathryn Dannemann, S. Chocron, A. Nicholls, J. Walker, C. Anderson, Compression testing and response of SiC-N ceramics: intact, damaged and powder, Proceedings of Advanced Ceramics and Composites Conference, January 23-28, 2005, Cocoa Beach, Florida

2. Sidney Chocron, Kathryn A. Dannemann, Arthur E. Nicholls, James D. Walker, Charles E. Anderson, A Constitutive Model For Damaged And Powder Silicon Carbide, Proceedings of Advanced Ceramics and Composites Conference, January 23-28, 2005, Cocoa Beach, Florida

3. Kathryn Dannemann, A. Nicholls, C. Anderson, S. Chocron, J. Walker, Response and Characterization of Confined Borosilicate Glass: Intact and Damaged, Proceedings of Advanced Ceramics and Composites Conference, January 23-27, 2006, Cocoa Beach,

4. ARL, private communication, 2005

REACTION SINTERED LiAlON

Raymond A. Cutler and R. Marc Flinders
Ceramatec, Inc.
2425 South 900 West
Salt Lake City, Utah 84119

ABSTRACT

Recent results suggest that Li^+ can substitute for Al^{3+} in the gamma-AlON structure. $LiAl_5O_8$ is isostructural with gamma-AlON above 1290°C after it goes through an ordered-disordered phase transformation and has a similar lattice parameter. A previous study showed the benefits of reaction sintering LiAlON starting with $LiAl_5O_8$ as compared to using Li_2O. The present study compared Li_2O, $LiAlO_2$, $LiAl_5O_8$, and $LiAl_{11}O_{17}$ at identical lithium levels when reaction sintering LiAlON using Al_2O_3 and AlN as the other reactants. X-ray diffraction was used to monitor phase changes as a function of sintering temperature. LiAlON formed by 1550°C in all lithium containing materials, with nearly full conversion by 1650°C, while AlON did not form until 1750°C under identical sintering conditions for the material without lithium. The starting source of the lithium did not control the ability to form LiAlON as was previously hypothesized. Lithia or lithium aluminate additions, however, are advantageous for reaction sintering Al_2O_3 and AlN since the volume expansion during sintering is avoided.

INTRODUCTION

LiAlON was recently reported by Clay, et al.[1] as a solid solution where Li^+ substitutes for Al^{3+} creating cation vacancies at low lithium levels. McCauley[2,3] and Corbin[4] pioneered reaction sintering work on AlON nearly thirty years ago where Al_2O_3 and AlN react to form a cubic spinel structure

$$\left(\frac{4-x}{3}\right)Al_2O_3 + xAlN \rightarrow Al_{\frac{(8+x)}{3}}V_{Al\left(\frac{1-x}{3}\right)}O_{4-x}N_x \qquad (1)$$

creating Al cation vacancies to allow charge neutrality. Al_2O_3, $LiAl_5O_8$, and AlN were reaction sintered. If all of the lithia were to leave the sample during reaction sintering, then the reaction is simply given as:

$$\left(\frac{8-2x}{15}\right)LiAl_5O_8 + xAlN \rightarrow Al_{\frac{(8+x)}{3}}V_{Al\left(\frac{1-x}{3}\right)}O_{4-x}N_x + \left(\frac{4-x}{15}\right)Li_2O\uparrow \qquad (2)$$

The work of Clay, et al.[1], however, indicated that all of the lithia did not leave the sample. Electroneutrality for cation vacancy formation, V^c, requires that if x and y range between 0 and 1 in

$$\left(Li_yAl_{(1-y)}\right)_{3-z}V_z^cO_{4-x}N_x \qquad (3)$$

then $z=\frac{1-x-6y}{3-2y}$. An analogous requirement for anion vacancy formation was proposed and could be expected to dominate at higher levels of lithia.[1] However, the most intriguing aspect of the work of Clay, et al.[1] was the possibility that the disordered high-temperature phase of $LiAl_5O_8$, which is isostructural with γ-AlON above 1290°C,[5] could act as a nucleation site for the spinel formation when AlN and Al_2O_3 are reaction sintered. Since it is well understood that anion diffusion is rate controlling in the reaction sintering of AlON[6] it is of interest to see

whether the presence of $LiAl_5O_8$ affects the reaction kinetics. The objective of this work was to determine if there is any advantage in using zeta alumina ($LiAl_5O_8$) when forming LiAlON, as compared to Li_2O or other lithium aluminates. Reaction-sintered AlON formed using 25 mol. % AlN was therefore compared with reaction-sintered LiAlON where the AlN content remained constant at 25 mol. % while some of the Al_2O_3 was replaced with Li_2CO_3, $LiAlO_2$, or $LiAl_5O_8$ keeping the lithium content constant. The β-alumina-like composition $LiAl_{11}O_{17}$, which is reported to be stable between 1750 and 1970°C,[7] is unquenchable and therefore consists of $LiAl_5O_8$ and Al_2O_3 at room temperature. $LiAlO_2$ is stable to 1785°C,[7] but will react with Al_2O_3 to form $LiAl_5O_8$ at elevated temperature. Understanding these limitations, this work was undertaken in an effort to understand whether the enhanced optical transparency for LiAlON compared with AlON compositions made under identical conditions,[1] was merely the enhanced grain growth or was influenced by the isostructural zeta alumina at elevated temperatures.

EXPERIMENTAL PROCEDURES

$LiAlO_2$, $LiAl_5O_8$, and "$LiAl_{11}O_{17}$" were prepared by reacting appropriate amounts of Li_2CO_3 (Aldrich grade 25,582-3) and Al_2O_3 (Sasol North America grade SPA-0.5) using polyvinyl pyrrolidone (PVP) as a dispersant in isopropanol as described previously.[1] The powders were vibratory milled for 72 hours with Y-TZP media inside high density polyethylene (HDPE) containers prior to calcining the dried powder at 1000°C for 10 hours. The calcined powders were milled an additional 72 hours with surface areas of 7.8, 8.7, and 10.7 m^2/g for the $LiAlO_2$, $LiAl_5O_8$, and "$LiAl_{11}O_{17}$" powders, respectively. The $LiAlO_2$ and $LiAl_5O_8$ were single-phase based on X-ray diffraction while the "$LiA_{11}O_{17}$" powder was composed as $LiAl_5O_8$ and Al_2O_3, as expected.

Five compositions, as listed in Table I, were prepared at 25 mol. % AlN, with four of the materials having identical lithium concentrations and the control sample without any lithium addition. The AlN and Al_2O_3 powders were the same grades as used in making the $LiAlO_2$, $LiAl_5O_8$, and "$LiA_{11}O_{17}$" additives. The powders were vibratory milled for 72 hours with 0.5 wt. % PVP dispersant in 70 grams reagent grade isopropanol in HDPE containers. The powders were dried and then slurried in hexane with 2 wt. % paraffin, based on the solids contents of the Table I compositions, before stir drying and screened through a nylon sieve. The lubricated powders were pressed uniaxially at 35 MPa followed by isostatic pressing at 250 MPa. The paraffin and dispersant were removed by heating in air to 600°C for one hour. Green dimensions after debinderization were approximately 31 mm in diameter by 5 mm in thickness, with green densities ranging between 2.2 and 2.3 g/cc for all compositions.

Table I
Compositions Prepared

Code	Mass (g)					
	AlN	Al_2O_3	Li_2CO_3	$LiAlO_2$	$LiAl_5O_8$	"$LiAl_{11}O_{17}$"
Control	17.52	130.72	---	---	---	---
Li_2O	17.52	130.72	4.11	---	---	---
$LiAlO_2$	17.52	125.06	---	7.33	---	---
$LiAl_5O_8$	17.52	102.48	---	---	30.00	---
$LiAl_{11}O_{17}$	17.52	68.42	---	---	---	64.01

Sintering was carried out in pyrolytic BN crucibles with parts packed in powder. The powder bed was a mixture of 25 wt. % BN and 75 wt. % AlON formed by reacting alumina and aluminum nitride. The purpose of the BN was to keep the AlON from sintering together. The purpose of the packing powder was to protect the AlON from the graphite in the furnace and to reduce the tendency for the material to volatilize. Sintering temperatures ranged from 1250-2050°C with one hour isothermal holds. A slight overpressure (0.5 atm) of nitrogen was applied above 1250°C.

Density was measured using the Archimedes' method. Rietveld analysis[8,9] was used to determine phases present in the densified samples with X-ray diffraction patterns collected from 15-75° 2Θ using Cu K_α radiation. Scanning electron microscopy was used to assess grain size and fracture mode.

RESULTS AND DISCUSSION

Figure 1 shows the linear shrinkage, density, open porosity, and weight loss as a function of sintering temperature. In accord with the results of Clay et al.[1], the control sinters more rapidly than the sample containing zeta alumina, with densification of the Al_2O_3-AlN occurring prior to the transformation to γ-AlON. The primary densification of the control sample has occurred by 1550°C. The 5.0 % volume expansion expected due to Reaction (1) is clearly evident in both the shrinkage and density measurements between 1650 and 1750°C, as shown in Figure 1.

Lithia additions, regardless of the source, slow down the sintering kinetics dramatically. Sintering using the "$LiAl_{11}O_{17}$" additive is slightly faster above 1350°C than with the other lithium-containing additives. No expansion is noted when lithia is present since the slower kinetics permits conversion to the spinel structure prior to final densification. This is advantageous for making large parts, such as armor, where large volume changes can induce cracking. Weight loss measurements indicated that all of the compositions retained most of their lithia at 1850°C, as the theoretical loss was 1.1 %. When the weight loss associated with volatilization of the control was factored in, 80-90 % of the lithia remains in compositions sintered at 1850°C using $LiAlO_2$, $LiAl_5O_8$, or "$LiAl_{11}O_{17}$" additives.

Lejus and Collongues[5] showed that cubic $LiAl_5O_8$ undergoes an order-disorder phase transformation at 1290°C from the ordered low-temperature phase (space group $P4_332$ with a=7.908Å) to the disordered high-temperature phase (space group Fd3m with a=7.925Å). The eutectoid decomposition temperature reported in the literature for AlON varies with Willems et al.[10] determining it to be 1640±10°C, Hillert and Jonsson[11] calculating it to be 1627°C, Qui and Metselaar[12] lowering the value to 1612°C, and Nakao, et al.[13] measuring 1630±4°C. In any event, by monitoring differences in X-ray diffraction between 1250 and 1350°C, where the order-disorder transformation occurs, and between 1550 and 1650°C, where the γ-AlON phase becomes stable, it should be possible to tell whether zeta alumina influences the phase stability of AlON or whether the addition of lithium simply enhances grain growth, which results in enhanced transparency as discussed by Clay et al.[1]

Figure 2 shows X-ray patterns for the five materials as a function of sintering temperature. Heating to 1250°C was sufficient to allow the Li_2CO_3 and $LiAlO_2$ to react with the alumina so that the compositions showed similar phases, as evidenced by the Rietveld data in Figure 3. No Li_2O or $LiAlO_2$ were identified by XRD, although some free ZrO_2, due to milling contamination and $Al(OH)_3$, likely due to reaction with water during density measurements, were

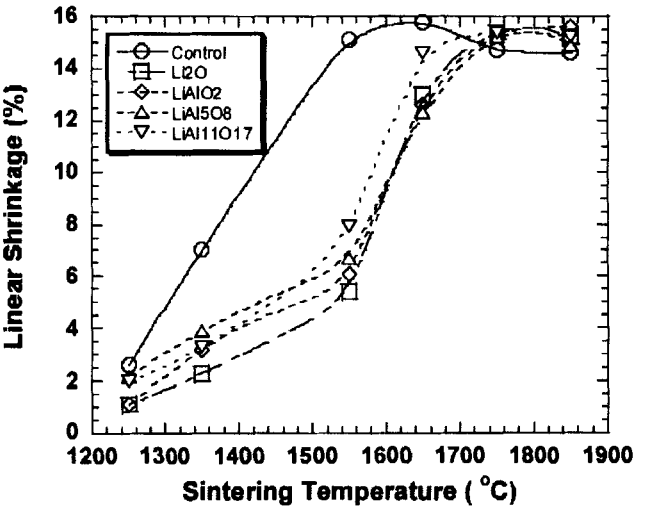

(a)

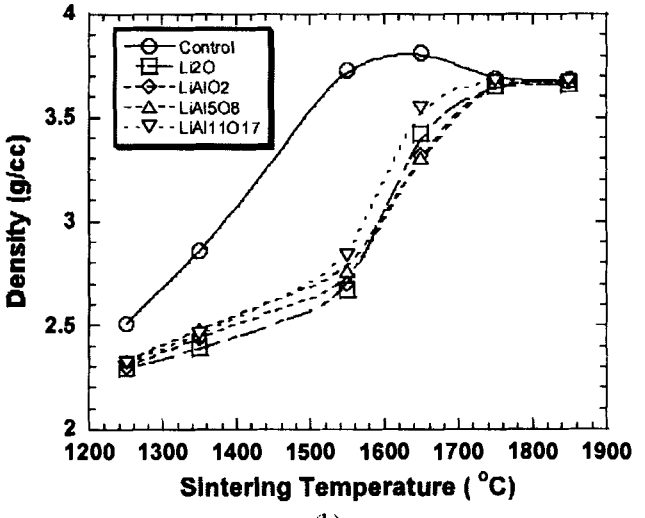

(b)

Figure 1. Linear shrinkage, density, open porosity, and weight loss as a function of sintering temperature. (a) Linear shrinkage, and (b) density.

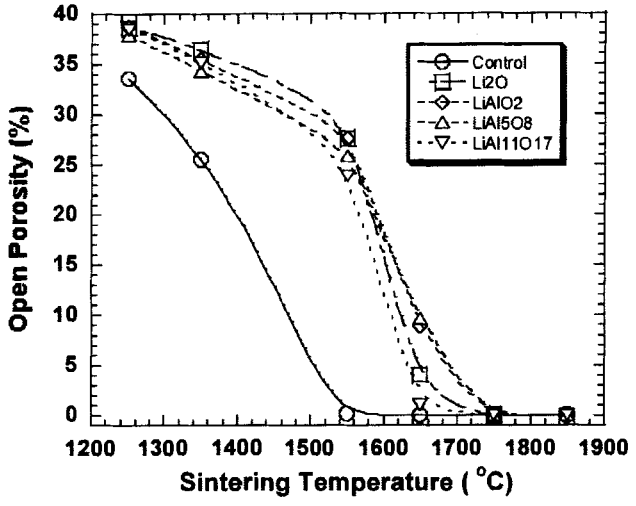

(c)

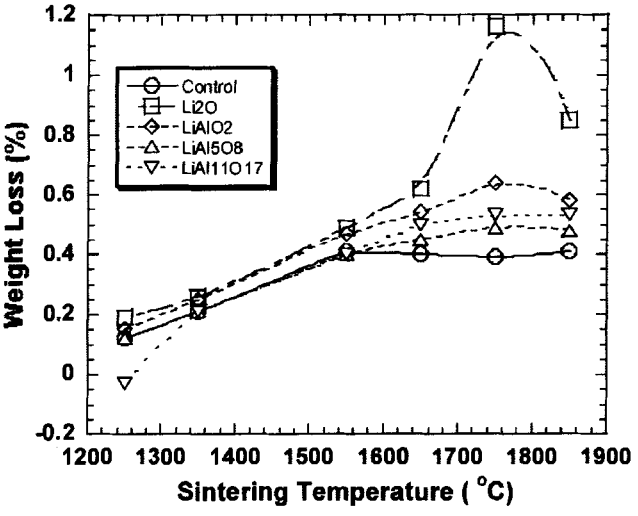

(d)

Figure 1 (continued). Open porosity (c) and weight loss (d) as a function of sintering temperature.

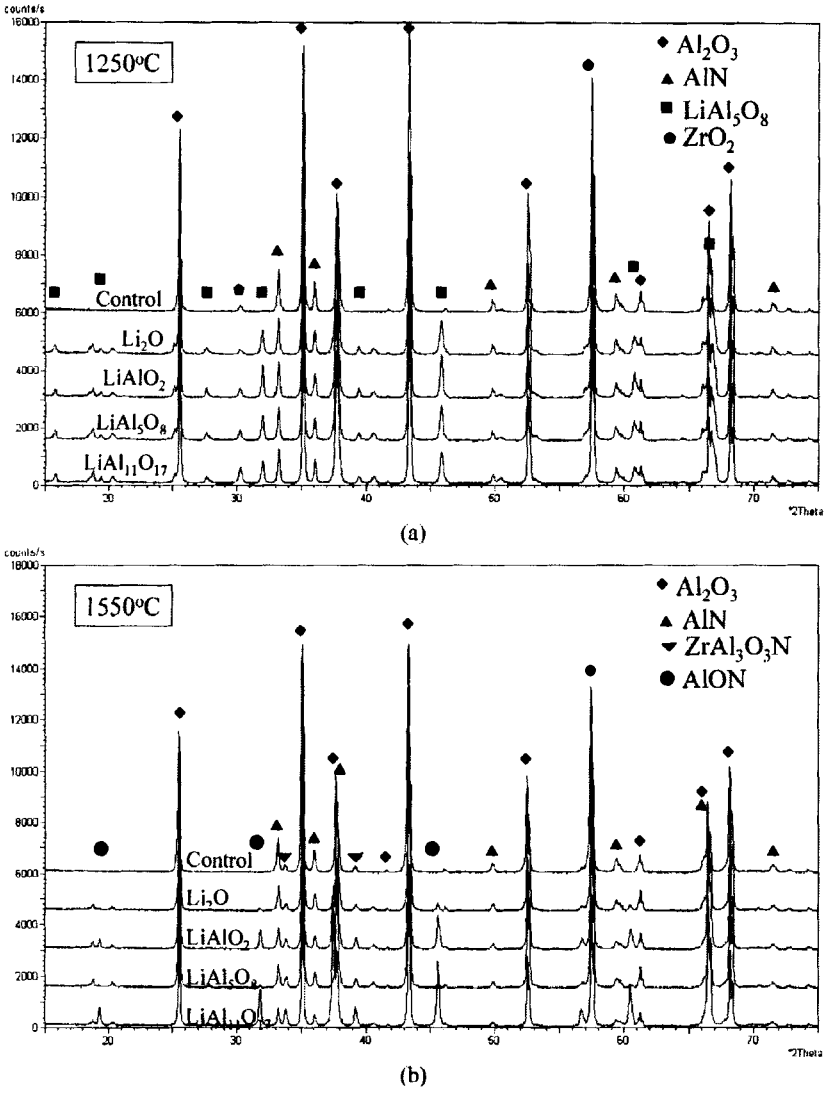

Figure 2. X-ray diffraction patterns of Table I compositions after sintering at the temperatures indicated. (a) 1250°C, and (b) 1550°C.

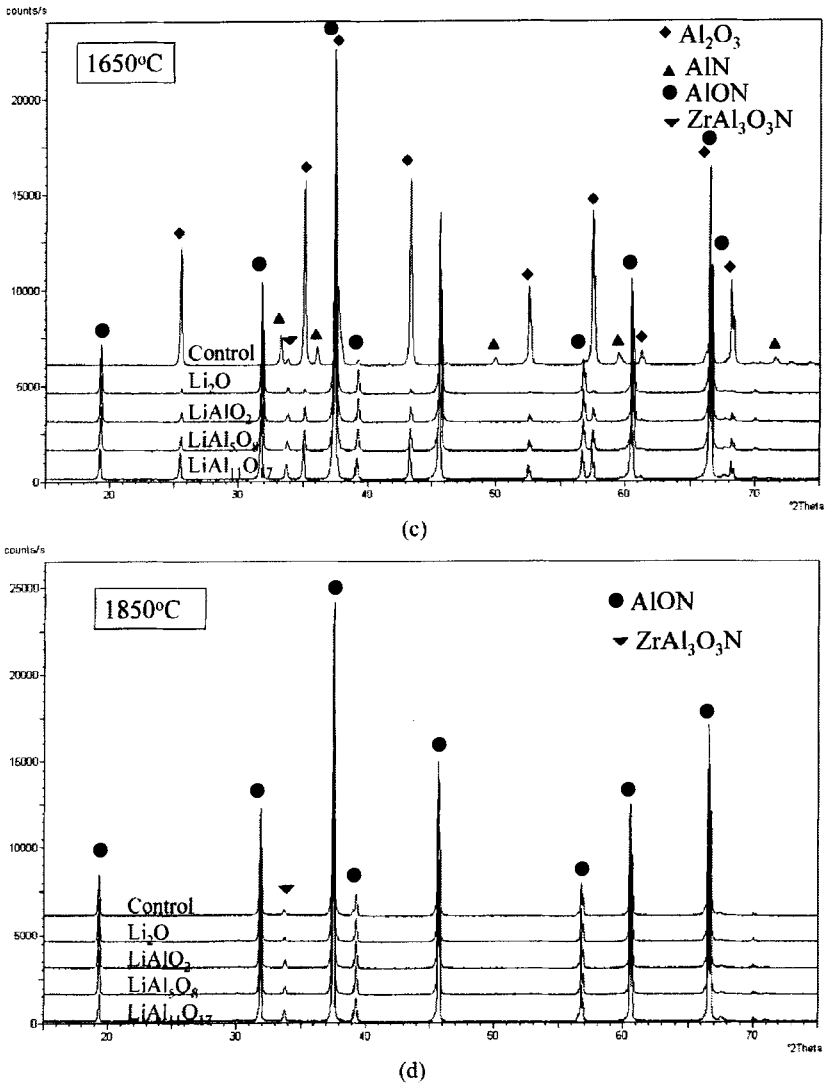

Figure 2 (continued). XRD patterns for samples sintered at (c) 1650°C or (d) 1850°C.

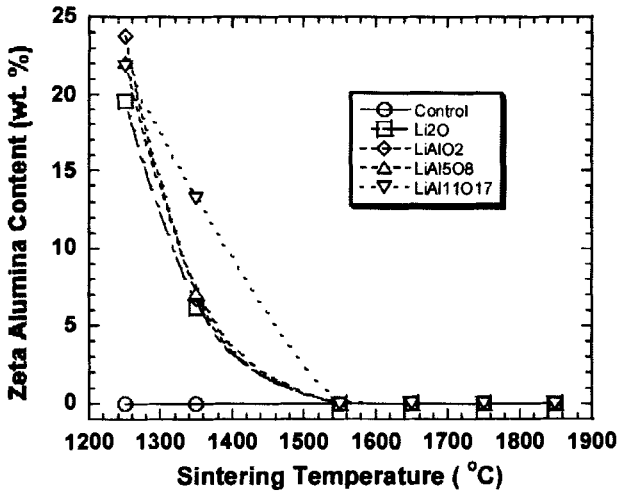

(a)

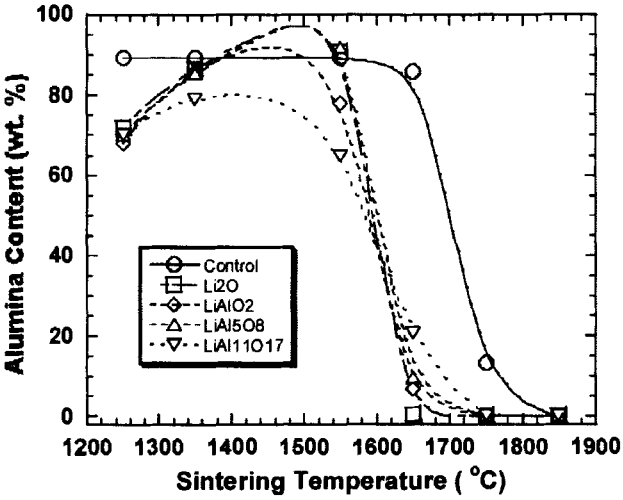

(b)

Figure 3. Rietveld fitting of XRD data showing phases present as a function of temperature. (a) $LiAl_5O_8$, and (b) Al_2O_3.

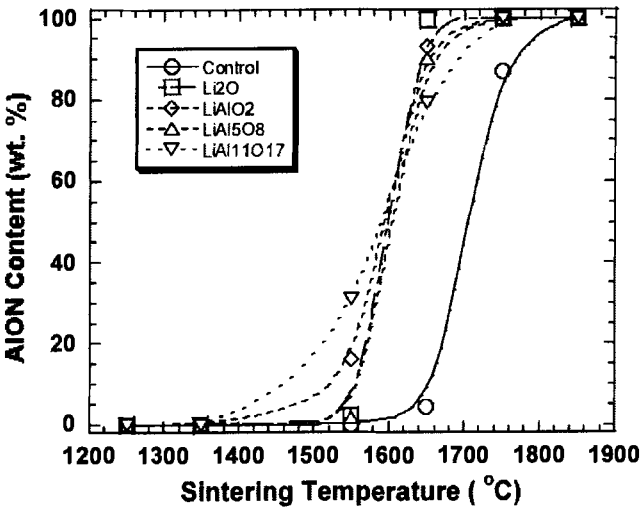

(c)

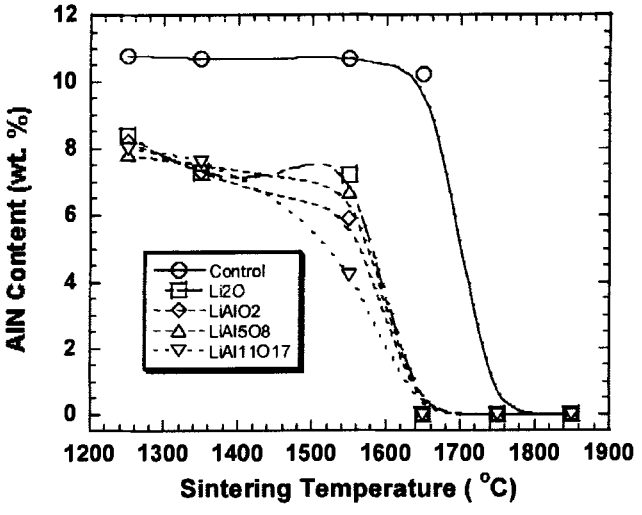

(d)

Figure 3 (continued). Rietveld fitting of AlON (c) and AlN (d) contents.

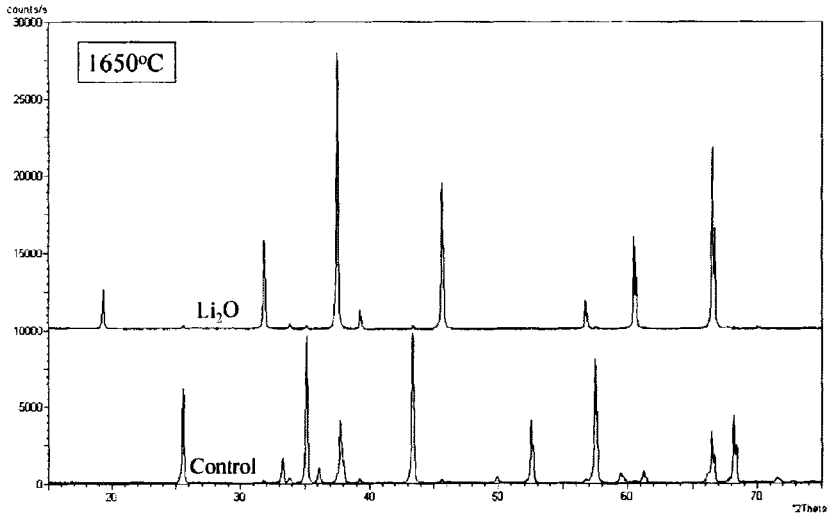

Figure 4. XRD patterns for reaction-sintered samples at 1650°C showing the difference in phases present between the two materials. The upper curve containing Li_2O has little Al_2O_3 and consists primarily of LiAlON whereas the bottom curve still consists of Al_2O_3 and AlN consistent with the data shown in Figure 1.

obvious in the 1250°C pattern. This resulted in all four lithium-containing materials having similar behavior, consistent with Figure 1.

Surprisingly, the amount of zeta alumina decreased upon heating to 1350°C, as shown in Figure 3(a), at the expense of increased alumina (see Figure 3(b)). The expectation was that the disordered $LiAl_5O_8$ phase, which is stable above 1290°C, would result in additional zeta alumina, or at least the same amount, for the samples sintered at 1350°C. Zeta alumina decreased with increasing temperature and was completely gone at 1550°C. However, by 1550°C, well below the reported stability temperature for AlON, it was obvious that the lithium containing materials allowed the LiAlON to form (see Figure 2(b) and Figure 3(c)). When heating to 1650°C, where the AlON is kinetically hindered from forming in the control sample, as shown in Figures 2(c) and 3(c), it was obvious that there was a difference between LiAlON and AlON samples. This difference is illustrated in Figure 4, which compares the control sample without lithium additions with the sample made using lithium carbonate. Heating to 1750°C results in conversion to AlON or LiAlON with the exception of the ZrO_2, which reacts top form an oxynitride upon heating above 1350°C. JCPDS card 48-1638 ("$ZrAl_3O_3N$") gave a good fit for the zirconium-containing phase.

Fracture surfaces of the samples sintered at 1850°C are displayed in Figure 5 using backscattered imaging, which reveals the grain size. Surprisingly, the control sample had a larger grain size than the lithium-containing materials as well as showed more transgranular fracture. The difference in fracture mode may be the result of grain size or may simply be affected by the zirconia contaminates, which precipitate out at grain boundaries. It is obvious

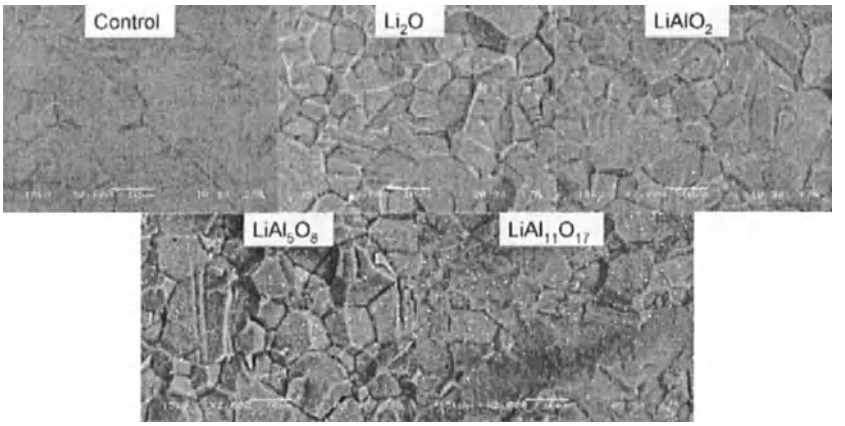

Figure 5. SEM images of fracture surfaces from the samples sintered at 1850°C showing that the grain size is larger in the control material than in the lithium containing materials.

that the milling was too aggressive and that high-purity alumina media rather than zirconia balls should have been used for the powder processing. The grain size of the control sample is larger than 10 μm whereas the lithium-containing materials all have grain size less than 10 μm. It therefore appears that the lithium can stabilize the AlON structure by going into solid solution. The starting lithium source is not important in this processing route, which results in zeta alumina as an intermediate compound in all applications. The mechanism for the stabilization is not apparent from the XRD and sintering data.

CONCLUSIONS

Reaction sintering with a variety of lithium-containing starting powders resulted in LiAlON formation below 1600°C, whereas transformation to AlON was observed at temperatures in excess of 1650°C. While zeta alumina was a precursor for all of the lithium containing materials, it was not apparent that the order-disorder transformation to the Fd3m space group was important for the $LiAl_5O_8$ as the amount of the material decreased between 1250 and 1350°C. A small amount of zeta alumina, however, may enhance the formation of LiAlON. Contrary to expectation, the lithium-containing materials were finer-grained than the material with no lithium added although zirconia contamination from the milling media may have influenced the results. By 1850°C, all materials showed similar XRD patterns. The major advantage of adding lithia or lithium aluminate to the starting composition is the ability to use a reaction sintering approach without full densification occurring prior to the volume expansion associated with the transformation.

ACKNOWLEDGEMENT

Appreciation is expressed to Lyle Miller and Angela Anderson of Ceramatec for help with X-ray diffraction work and density measurements, respectively.

REFERENCES

[1]D. Clay, D. Poslusny, M. Flinders, S. D. Jacobs, and R. A. Cutler, "Effect of $LiAl_5O_8$ Additions on the Sintering and Optical Transparency of LiAlON," *J. Eur. Ceram. Soc.*, **26**, 1351-62 (2006).

[2]J. W. McCauley, "A Simple Model for Aluminum Oxynitride Spinels," *J. Am. Ceram. Soc.*, **61**[7-8], 372-73 (1978).

[3]J. W. McCauley, and N. D. Corbin, "Phase Relations and Reaction Sintering of Transparent Cubic Aluminum Oxynitride Spinel (ALON)," *J. Am. Ceram. Soc.*, **62**[9-10], 476-79 (1979).

[4]N. D. Corbin, "Aluminum Oxynitride Spinel: A Review," *J. Eur. Ceram. Soc.*, **5**[3], 143-54 (1989).

[5]A. M. Lejus and R Collongues, "The Structure and Properties of Lithium Aluminates," *Compt. Rend.*, **254**, 2005-7 (1962).

[6]S. Bandyopadhyay, G. Rixecker, F. Aldinger, S. Pal, K. Mukherjee, and H. S. Maiti, "Effect of Reaction Parameters on γ-AlON Formation from Al_2O_3 and AlN," *J. Am. Ceram. Soc.*, 84[4], 1010-12 (2002).

[7]L. P. Cook and E. R. Plante, "Phase Diagram for the System Lithia-Alumina," *Ceram. Trans.* **27**, 193-222 (1992).

[8]H. M. Rietveld, "A Profile Refinement Method in Neutron and Magnetic Structures," *J. Appl. Crystallogr.*, **2**, 65-71 (1969).

[9]D. L. Bish and S. A. Howard, "Quantitative Phase Analysis Using the Rietveld Method," *J. Appl. Crystallogr.*, **21**, 86-91 (1988).

[10]H. X. Willems, M. M. R. M. Hendrix, G. de With, G. and R. Metselaar, "Thermodynamics of AlON II: Phase Relations," *J. Mater. Sci.*, **10**, 339-46 (1992).

[11]M. Hillert and S. Jonson, "Thermodynamic Calculation of the Al-N-O System," *Z. Metallkd.*, **83**[10], 714-19 (1992).

[12]C. Qui and R. Metselaar, "Phase Relations in the Aluminum Carbide-Aluminum Nitride-Aluminum Oxide System," *J. Am. Ceram. Soc.*, **80**[8], 2013-20 (1997).

[13] W. Nakao, H. Fukuyama, and K. Nagata, "Thermodynamic Stability of γ-Aluminum Oxynitride," *J. Electrochem. Soc.*, **150**[2], J1-J7 (2003).